The Astrophysical Journal, 953:115 (14pp), 2023 August 10 https://doi.org/10.3847/1538-4357/ace104

The Effects of Self-interacting Bosonic Dark Matter on Neutron Star Properties

Edoardo Giangrandi[1], Violetta Sagun[1], Oleksii Ivanytskyi[2], Constança Providência[1], and Tim Dietrich[3,4]
[1] CFisUC, Department of Physics, University of Coimbra, Rua Larga P-3004-516, Coimbra, Portugal
[2] Incubator of Scientific Excellence—Centre for Simulations of Superdense Fluids, University of Wrocław, 50-204, Wroclaw, Poland
[3] Institut für Physik und Astronomie, Universität Potsdam, Haus 28, Karl-Liebknecht-Str. 24/25, Potsdam, Germany
[4] Max Planck Institute for Gravitational Physics (Albert Einstein Institute), Am Mühlenberg 1, Potsdam D-14476, Germany
Received 2022 September 27; revised 2023 June 21; accepted 2023 June 21; published 2023 August 9

Abstract

We propose a model of asymmetric bosonic dark matter (DM) with self-repulsion. By adopting the two-fluid formalism, we study different DM distribution regimes, either, fully condensed inside the core of a star, or, otherwise, distributed in a dilute halo around a neutron star (NS). We show that for a given total gravitational mass, DM condensed in a core leads to a smaller radius and tidal deformability compared to a pure baryonic star. This effect may be interpreted as an effective softening of the equation of state. On the other hand, the presence of a DM halo increases the tidal deformability and total gravitational mass. As a result, an accumulated DM inside compact stars could mimic an apparent softening/stiffening of strongly interacting matter EoS and constraints we impose on it at high densities. We limit the model parameter space by confronting the cross section of the DM self-interaction to the constraint extracted from the analysis of the Bullet Cluster. Furthermore, from the analysis of the effect of DM particles, interaction strength, and relative DM fractions inside NSs we obtained a rigorous constraint on model parameters. To identify its impact on NSs we consider the DM fraction may reach up to 5%, which could be considered too high in several scenarios. Finally, we discuss several pieces of smoking gun evidence of the presence of DM that is free from the abovementioned degeneracy between the effect of DM and properties of strongly interacting matter. These signals could be probed with future and ongoing astrophysical and gravitational wave surveys.

Unified Astronomy Thesaurus concepts: Neutron stars (1108); Dark matter (353); Gravitational waves (678)

1. Introduction

Since the first detection of the binary neutron star (NS) merger, GW170817 (Abbott et al. 2017a), which was accompanied by the observation of electromagnetic signals originating from the same source, GRB170817A and AT2017gfo (Abbott et al. 2017b), we have been witnessing exciting breakthroughs in our understanding of compact stars and their merger dynamics. In fact, gravitational wave (GW) astronomy and multi-messenger astrophysics became new tools to extract information about the internal structure of NSs from GW and electromagnetic observations (Bauswein et al. 2017; Annala et al. 2018; Hinderer et al. 2019). Thus, from the combined analysis of the GW170817 signal measured by the advanced LIGO and advanced Virgo detectors, the constraint on the tidal deformability parameter of NS matter $\Lambda_{1.4} \leqslant 800$ was extracted (Abbott et al. 2018). The second binary NS merger event, GW190425 (Abbott et al. 2020a), provided constraints consistent with GW170817, but due to its lower signal-to-noise ratio did not deepen our knowledge about the NS equation of state (EoS). In addition to GW observations, also X-ray observations by NICER (Miller et al. 2019, 2021; Riley et al. 2019, 2021; Raaijmakers et al. 2020), radio measurements of the heaviest pulsars, e.g., PSR J0348+0432 of mass $2.01 \pm 0.04\ M_{\odot}$ (Antoniadis et al. 2013), PSR J0740 +6620 of $2.08^{+0.07}_{-0.07}\ M_{\odot}$ (Fonseca et al. 2021), and optical observations of the *black widow* pulsars, e.g., PSR J1810 +1744 of $2.13 \pm 0.04\ M_{\odot}$ (Romani et al. 2021), and PSR J0952-0607 of $2.35 \pm 0.17\ M_{\odot}$ (Romani et al. 2022) constrain the properties of NSs.

While all the mentioned analyses and models assume that NSs are embedded in a pure vacuum and do not contain dark matter (DM), they, indeed, could accumulate a sizable amount of DM in their interior and surroundings. Due to high compactness, NSs can effectively trap DM particles, which will rapidly thermalize and become accrued inside the stars, altering their properties. The presence of DM affects the internal structure and compactness of compact stars. Thus, as was shown, e.g., in Ciarcelluti & Sandin (2011), Ellis et al. (2018b), Nelson et al. (2019), Ivanytskyi et al. (2020), Das et al. (2020b), and Sagun et al. (2022), DM may either form an extended halo or a dense core inside an NS. Depending on the mass of DM particles, their self-interaction strength, and its relative abundance inside the star, one of the abovementioned scenarios takes place. Since DM halos are invisible for typical astrophysical observations, we would see only the baryonic matter (BM) radius, independent of the fact that the outermost radius can extend further than its BM component (Karkevandi et al. 2022). On the contrary, a DM core formation will lead to a reduction in the NS radius.

Moreover, DM will affect tidal deformability parameters and merger dynamics (Ellis et al. 2018a; Bezares et al. 2019; Leung et al. 2022; Bauswein et al. 2023). Nowadays, while there are studies investigating possible alternative scenarios beyond *standard* compact binary mergers described by general relativity in pure vacuum (Abbott et al. 2019a), the models used to analyze GW signal do not account directly for DM.

Thus, to understand the effect of DM on the coalescence of NSs, numerical-relativity simulations for different DM fractions, particle mass, and interaction strength are required

(Rüter et al. 2023). As a step in this direction, there have been the first two-fluid 3D simulations of coalescing binary NS admixed with DM with the following studies of GW emission of the merger remnant, e.g., Bauswein et al. (2023) and Emma et al. (2022). By considering different binary masses and EoSs, Bauswein et al. (2023) showed that the GW frequency of the orbiting DM components scales with the compactness of NSs. Moreover, the relations between the DM GW frequency and the dominant post-merger GW frequency of the stellar fluid or the tidal deformability were found, which opens a possibility to probe the EoS effects during the binary inspiral. Emma et al. (2022) studied the effect of mirror DM concentrated inside the core on the deceleration of the inspiral phase, as well as on a modification of the ejecta and debris disk formation.

Depending on whether DM has particle-antiparticle asymmetry, we will refer to it as asymmetric or symmetric matter. Symmetric DM particles can self-annihilate leaving a possibility of its detection via X-ray, γ-ray, or neutrino telescopes (Kouvaris 2008). Moreover, as studied in Pérez-García & Silk (2012), self-annihilating DM in the inner regions of NSs may have a significant impact on the kinematic properties, namely, velocity kicks and rotation patterns.

Another possible effect of DM particle annihilation inside the NS core is related to the late-time heating, which could be detected from observations of the surface temperature of the old part of the NS population (de Lavallaz & Fairbairn 2010; Hamaguchi et al. 2019). Unfortunately, nowadays, our database of old NSs is still quite limited.

Contrary to the annihilating DM, asymmetric DM will become accumulated inside a star. Models that consider such a scenario should allow old NSs to exist. Especially, it is important for bosonic DM particles, which at zero temperature could form Bose–Einstein condensate (BEC) leading to the gravitational collapse of the bosonic DM to a black hole (Kouvaris 2013).

Light DM particles, such as axions, could contribute as an additional cooling channel in compact stars. Thus, in the NS core axions can be produced either in nucleon bremsstrahlung or in Cooper pair breaking and formation processes (Sedrakian 2016, 2019; Buschmann et al. 2022), causing an alteration of the surface temperature and thermal evolution of a star. In addition, most of the existing models are constrained by the results of neutrino emission coming from the supernova observation SN 1987A (Chang et al. 2018) and existing NS cooling data. The results of NS merger simulations (Dietrich & Clough 2019) show that axions produced in nucleon–nucleon bremsstrahlung do not lead to a measurable change in the emitted GW signal, ejecta mass, as well as the temperature profile of the merger remnant.

The fraction of DM in the compact star interior depends on different factors. Thus, DM can be captured by NSs from the surrounding medium. Following scattering processes, the kinetic energy of DM particles is transferred to the star (Kouvaris 2013; Bell et al. 2020, 2021), and becomes gravitationally bound with a star. The amount of DM accrued by an ordinary accretion throughout a stellar evolution will depend on the position of the considered NS in the Galaxy (Kouvaris & Tinyakov 2010). As the DM density in the Galactic Center is many orders of magnitude greater than in its arms, we may expect a higher DM fraction in compact stars toward the Milky Way center (Del Popolo et al. 2020). Furthermore, NSs in globular clusters may contain a significant amount of DM (Bertone & Fairbairn 2008). Moreover, we should not forget that NS is the final stage of star's evolution preceded by the progenitor, main-sequence star, and supernova explosion with the formation of a proto-NS. These and all other mechanisms are discussed in detail in Karkevandi et al. (2022). As was estimated by Ivanytskyi et al. (2020), the amount of accumulated DM in the most central part of the Galaxy accrued by a spherically symmetric accretion scenario during the main-sequence star and equilibrated NS stages is 0.01%. However, additional scenarios could lead to high DM factions inside compact stars, e.g., DM production during a supernova explosion, accretion of DM clumps formed at the early stage of the universe, or initial star formation on a preexisting dark core. As we are interested in identifying possible signatures on NSs, we have concentrated our study on fractions up to 5%, which cannot be accumulated by a spherically symmetric DM accretion followed by thermalization via the interaction with BM, and requires the alternative mechanisms mentioned above.

Moreover, some local non-homogeneity of DM distribution may contribute to an increase in DM fraction, leading even to dark compact objects (Dengler et al. 2022) and dark stars (Kouvaris & Nielsen 2015; Maselli et al. 2017).

Since DM properties are still unknown, different models have been employed, considering its fermionic (Goldman et al. 2013; Gresham et al. 2017; Ivanytskyi et al. 2020) and bosonic (Colpi et al. 1986; Petraki & Volkas 2013; Karkevandi et al. 2022) nature. As it was discussed by Bramante et al. (2013) to be consistent with the observations of old NSs, bosonic DM has to be either self-interacting, decaying, or self-annihilating. Considering asymmetric DM a repulsive self-interaction is required due to zero degeneracy pressure. At the moment when accumulated bosonic asymmetric DM exceeds the Chandrasekhar mass, nothing can prevent its gravitational collapse and the formation of a black hole inside the NS, which could potentially disrupt the star (Kouvaris 2013; Zurek 2014).

Using an analog of visible matter and the Standard Model particles, we see that all interactions have an exchange character, an interaction between particles occurs due to an exchange of a mediator, e.g., the interaction between nucleons is mediated by pions. In the present article, we extend this approach for a dark sector by formulating a model of self-interacting asymmetric bosonic DM, which includes vector interaction mediated by a real ω-field coupled to the scalar one. We model DM-admixed compact stars by considering the mixed system of two fluids with different relative fractions.

The assumption of cold self-interacting DM provides a good agreement with the large-scale structure of the universe and cosmology. It reconciles the success of the cold DM (CDM) model with the non-observation of cuspy density profiles of dwarf galaxies predicted by CDM N-body simulations and known as the core-cusp problem (Moore 1994). In comparison to an alternative mechanism to flatten the central density profile by supernova-driven episodes of gas removal, self-interacting DM is a more favorable one (Burger et al. 2022). On the other hand, from the observed mass profiles of galaxies (Ahn & Shapiro 2005) and Bullet Cluster observations (Clowe et al. 2006; Randall et al. 2008) the DM self-interaction cross section per unit mass has an upper limit of $\sigma/m < 1.25\ \mathrm{cm}^2\ \mathrm{g}^{-1}$ (68% confidence level). The DM model considered in this paper is in line with the above assumption, and therefore, provides consistency with the state of the art of modern cosmology. Moreover, below we explicitly account for the above constraint

on σ/m in order to limit the model parameters. An implication of the proposed EoS and tests against astrophysical and GW observations are performed in this work.

The paper is organized as follows. In Section 2, we present models for the BM and DM components, with a detailed derivation provided in Appendix A. Section 3 is dedicated to the equilibrium configurations of DM-admixed compact stars. In Section 4, we discuss how the speed of sound and the tidal deformability are affected by the presence of DM. In Section 5 the main results are presented, including the constraints on mass and interaction scale of DM particles. In Section 6, we discuss the smoking gun signals of the presence of DM that could be tested in the nearest future before concluding in Section 7. In Appendix A, we show the full derivation of the DM EoS, with a focus on the effective speed of sound for a DM-admixed NS in Appendix B. In Appendix C, we show the scan over the model parameters and the obtained constraints. Throughout the article, we utilize a unit system in which $\hbar = c = G = 1$.

2. Models of Dark and Baryonic Matter

2.1. DM EoS

We consider the model of massive spinless DM particles carrying a conserved charge. Such particles are described by a complex scalar field, and have mass m_χ and chemical potential μ_χ. At sufficiently low temperatures bosonic DM exists in the form of the BEC. In the absence of interaction such BEC has zero pressure and is mechanically unstable against gravitational compression. We stabilize the BEC of DM by introducing repulsive interaction mediated by a real vector field coupled to the scalar one. The minimal Lagrangian representing this model is given in Appendix A. It is equivalent to a massive $U(1)$ gauge theory of scalar particles, i.e., scalar electrodynamics with massive photons. This Lagrangian implies a Noether current corresponding to the invariance of action with respect to global $U(1)$ transformations. If the vector field was not a Yukawa but a gauge one, local $U(1)$ symmetry would also be respected and another Noether current could be introduced (Brading & Brown 2000). Given a quantum treatment, expectation values of these two currents produce the same conserved charge, which is not the case within the used mean-field approximation corresponding to a classical treatment of the vector field (see Appendix A for details). We use the Noether current resulting from global $U(1)$ transformations, which leave the action invariant even at the mean-field level.

In this work, we assume the vanishing temperature of the DM, being totally converted to the BEC. In the considered case thermal fluctuations are suppressed and mean-field approximation can be applied in order to derive the corresponding EoS. Chemical potentials of the BM and DM components of NS scale proportionally (for more details see Section 3). This significantly simplifies solving two coupled Tolman–Oppenheimer–Volkoff (TOV)–like equations for BM and DM components, as shown by Ivanytskyi et al. (2020). Therefore, it is convenient to formulate the DM EoS in the grand canonical ensemble (GCE), where μ_χ is an independent variable. Appendix A includes details of the corresponding derivation for the interval of physical values of $\mu_\chi \in [0, \sqrt{2}m_\chi]$ performed in the locally flat spacetime, provided by small gradients of metrics and absence of the anisotropy issues (see Karkevandi et al. 2022 for details). The corresponding pressure and energy density are

$$p_\chi = \frac{m_I^2}{4}(m_\chi^2 - \mu_\chi\sqrt{2m_\chi^2 - \mu_\chi^2}), \tag{1}$$

$$\varepsilon_\chi = \frac{m_I^2}{4}\left(\frac{\mu_\chi^3}{\sqrt{2m_\chi^2 - \mu_\chi^2}} - m_\chi^2\right), \tag{2}$$

for $\mu_\chi \in [m_\chi, \sqrt{2}m_\chi]$ and $p_\chi = \varepsilon_\chi = 0$ for $\mu_\chi \in [0, m_\chi]$. The parameter m_I has the unit of mass and controls the interaction strength. It is proportional to the vector meson mass m_ω and inversely proportional to its coupling g. Thus, large m_I corresponds to weak interaction and vice versa. At first glance, the present EoS in the weak coupling regime paradoxically leads to an infinite pressure due to $m_I \to \infty$. This, however, is not the case since in the considered regime chemical potential of the DM BEC μ_χ coincides with its mass m_χ leading to the vanishing of the brackets in Equations (1) and (2). In the case of p_χ the bracket vanishes faster than m_I^2 yielding to a zero pressure $\sim m_I^{-2}$, while for ε_χ the bracket behaves as $\sim m_I^{-2}$ providing a finite energy density of the DM BEC $m_\chi n_\chi$. In the strong coupling regime, $m_I \to 0$ chemical potential of DM converges to $\sqrt{2}m_\chi$. As a result, the bracket in Equation (1) becomes equal to m_χ^2 and the pressure vanishes as $m_I^2 m_\chi^2/4$. The corresponding bracket in Equation (2) diverges as $\sim m_I^{-2}$ leading to finite energy density $\sqrt{2}m_\chi n_\chi$. Remarkably, weak and strong coupling limits of the present EoS are similar, since DM pressure vanishes in both these cases. At $m_I \to \infty$ it is due to the absence of repulsion. The limit $m_I \to 0$ is equivalent to the case of the massless vector field, which does not have a nontrivial mean-field solution needed to stiffen the EoS. Detailed analysis of the weak and strong coupling limits of the present EoS is performed in Appendix A.

A remarkable feature of the present EoS is that at infinite density its pressure is limited by the value $p_\infty = m_I^2 m_\chi^2/4$. This regime is reached at $\mu_\chi = \sqrt{2}m_\chi$. Thus, the compressibility of DM vanishes at asymptotically high densities regardless of m_χ and m_I. The same conclusion holds for the speed of sound $c_{s,\chi}^2 = dp_\chi/d\varepsilon_\chi$. In other words, high-density configurations of bosonic DM are gravitationally unstable at any strength of the repulsive interaction. The left panel of Figure 1 shows the pressure, energy density, and speed of sound of the considered DM EoS as functions of the corresponding chemical potential. It is worth mentioning, that the square of the speed of sound is limited from above by the value $1/9$, which is reached at $\mu_\chi = \sqrt{3/2}\ m_\chi$ and does not depend on m_χ and m_I. Thus, $c_{s,\chi}^2$ is bounded by quite small values and corresponds to the soft EoS of DM. The right panel of Figure 1 shows this EoS as a function of energy density.

Observational data on the colliding clusters of galaxies 1E 0657-56 (the Bullet Cluster) enable probing dynamics of the DM fluid on the cosmological scale. This dynamic is determined by the DM self-interaction, which is controlled by the corresponding cross section σ_χ. Evaluation of this quantity requires the invariant matrix element of scattering of two on-shell DM particles from the initial state with three momenta $\boldsymbol{k}_1$ and $\boldsymbol{k}_2$ to the final one with momenta $\boldsymbol{k}_1'$ and $\boldsymbol{k}_2'$. At the tree level, this matrix element includes contributions from the t- and u-channels

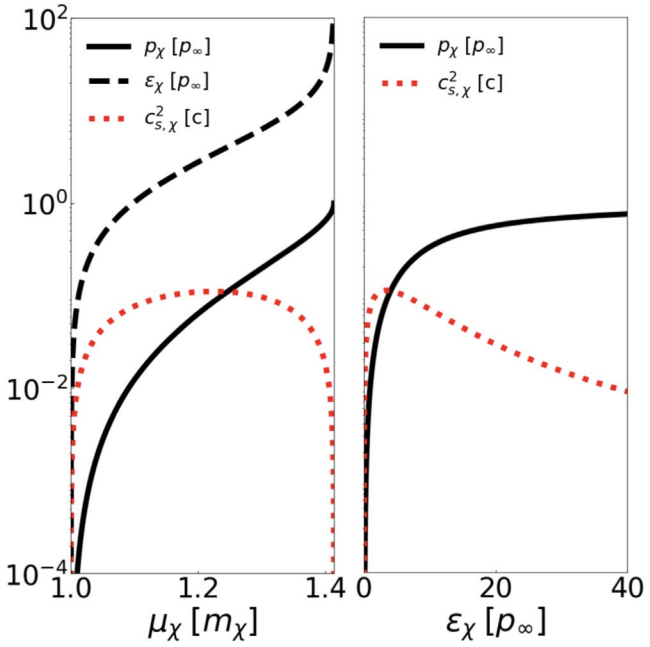

Figure 1. Left panel: scaled pressure p_χ/p_∞ (black solid curve), energy density $\varepsilon_\chi/p_\infty$ (black dashed curve), and speed of sound squared $c^2_{s,\chi}$ (red dotted curve) of DM as functions of its chemical potential μ_χ given in units of m_χ. Right panel: scaled pressure p_χ/p_∞ (black solid curve) and speed of sound $c^2_{s,\chi}$ (red dotted curve) of DM as functions of scaled energy density ε_χ given in units of p_∞.

independent of the angle variables. Therefore, the total one is obtained by multiplying $d\sigma_\chi/d\Omega$ by 4π. Finally, we obtain

$$\frac{\sigma_\chi}{m_\chi} = \frac{2m_\chi}{\pi m_I^4}. \tag{5}$$

Numerical simulations of the Bullet Cluster combined with the results from X-ray, strong and weak lensing, and optical observation set an upper limit on this ratio Randall et al. (2008). Within the 68% confidence interval $\sigma_\chi/m_\chi < 1.25\,\mathrm{cm}^2\,\mathrm{g}^{-1}$, while assuming equal mass-to-light ratios in the subcluster and the main cluster prior to the merger yields even more stringent constraint $\sigma_\chi/m_\chi < 0.7\,\mathrm{cm}^2\,\mathrm{g}^{-1}$. In order to keep the parameter space of the model as wide as possible, we use a more relaxed version of this constraint. Thus, we require

$$m_I\ [\mathrm{MeV}] > 18.24\ \sqrt[4]{m_\chi\ [\mathrm{MeV}]}\,. \tag{6}$$

This requirement obviously discredits the strong coupling limit $m_I \to 0$ with respect to the above cosmological constraint on the DM self-interaction cross section. Further analysis is limited to the region of the model parameter space, which respects Equation (6).

2.2. BM EoS

In order to thoroughly study the impact of DM on compact stars made of mostly BM, we consider two EoSs of different stiffness. One of them is the induced surface tension (IST) EoS,

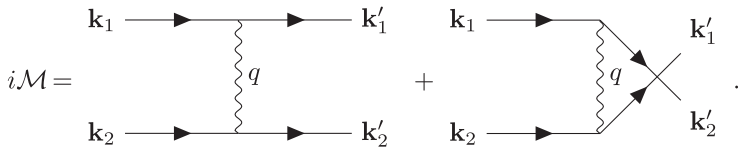

(3)

These diagrams are formalized by the Feynman rules of scalar quantum electrodynamics with massive photons. Each vertex corresponds to a factor $-ig$. The annihilation of a particle with four-momentum k and the creation of another one with four-momentum k' in a vertex produces the factor $-k_\mu - k'_\mu$, while in the case of antiparticles, the momenta entering this factor have the opposite signs. Wavy lines stand for the vector field propagator $-ig^{\mu\nu}(q^2 - m_\omega^2)^{-1}$ with q being a transferred momentum. The conservation of energy and momentum ensures that in the t- and u-channels, which are represented by the upper and lower graphs in Equation (3), squared transferred momentum coincides with the Mandelstam variables $t = (k_1 - k_1')^2 = (k_2 - k_2')^2$ and $u = (k_1 - k_2')^2 = (k_2 - k_1')^2$, respectively. The Lorentz indexes μ and ν appearing in the vertexes and in the vector field propagator are dummies. With this, we arrive at

$$\mathcal{M} = g^2\left[\frac{(k_1 + k_1')(k_2 + k_2')}{t - m_\omega^2} + \frac{(k_1 + k_2')(k_2 + k_1')}{u - m_\omega^2}\right]. \tag{4}$$

In the BEC case, three momenta of the incoming and outgoing particles vanish, which produces $4m_\chi^2$ in the numerator of each fraction in the previous expression and corresponds to $t = u = 0$. This yields $\mathcal{M} = -8m_\chi^2/m_I^2$ and differential cross section of the DM self-interaction $d\sigma_\chi/d\Omega = |\mathcal{M}|^2/64\pi^2 E_{\mathrm{cm}}$, where $E_{\mathrm{cm}} = 2m_\chi$ is the center-of-mass energy of the incoming particles with $\boldsymbol{k}_1 = \boldsymbol{k}_2 = 0$. This differential cross section is

formulated on the basis of the hard-core approach. Thus, nucleons are characterized by an effective hard-core radius that provides a short-range repulsion between the particles of different species. This part of the model was fixed from the fit of heavy-ion collision data (Sagun et al. 2018), while the IST contribution was implemented by accounting for an inter-particle interaction at high density. The corresponding parameters were fitted to reproduce the nuclear matter ground-state properties, correct behavior of the nuclear liquid–gas phase transition and its critical point (Sagun et al. 2017) and proton flow constraint (Ivanytskyi et al. 2018). Furthermore, in Sagun et al. (2019b) the model was generalized to describe NSs showing a big application range of the unified IST approach Sagun et al. (2019a). In the present work, we consider the Set B described in detail in Sagun et al. (2020), while the crust is modeled in a simplified way by the polytropic EoS with adiabatic index $\gamma = 4/3$. This model parameterization reproduces GW170817 and GW190425 tidal deformability limit (Abbott et al. 2018, 2020a), NICER mass–radius measurements (Miller et al. 2019, 2021; Riley et al. 2019, 2021; Raaijmakers et al. 2020), as well as the maximum mass constraint.

In addition, we consider the DD2 EoS (Typel & Wolter 1999; Typel et al. 2010) with and without Λ hyperons. The DD2 is a mean-field relativistic nuclear model with density-dependent couplings, whose parameters were fitted to the ground-state properties of nuclei. Hyperons have been included in several

works. In the present study, the density dependence of the hyperon couplings to the σ, ω, and ρ mesons are considered to be the same as one of the nucleons. For the ϕ coupling, the density dependence of the ω meson is considered. The couplings of the σ meson to the Λ and Ξ have been taken from Fortin et al. (2017, 2020), respectively, and have been fitted to the binding energy of Λ and Ξ hypernuclei. The coupling to the Σ hyperon was chosen so that the Σ potential in symmetric nuclear matter is +30 MeV, see Gal et al. (2016) for a discussion. For the vector mesons, the quark model predictions are used,

$$g_{\omega\Lambda} = g_{\omega\Sigma} = \frac{2}{3} g_{\omega N}, \quad g_{\omega\Xi} = \frac{1}{3} g_{\omega N},$$
$$g_{\phi\Lambda} = g_{\phi\Sigma} = -\frac{\sqrt{2}}{3} g_{\omega N}, \quad g_{\phi\Xi} = -\frac{2\sqrt{2}}{3} g_{\omega N}.$$

Finally, the effective ρ-meson coupling is determined by the product of the hyperon isospin with the ρ meson-nucleon coupling. The DD2 EoS without Λ hyperons reproduces the maximum mass constraint ($M_{\rm max} = 2.4 M_\odot$) and NICER data, while $\Lambda_{1.4}$ is 700. At the same time, the DD2 EoS with Λ hyperons gives the maximum mass of 2 $M_\odot$. Further on the DD2 EoS with Λ hyperons will be referred to as the DD2Λ.

The complete NS EoS contains, besides the core EoS, the BPS EoS Baym et al. (1971) for the outer crust, and the inner crust was calculated within a Thomas–Fermi calculation taking DD2 as the underlying model and allowing for the appearance of several geometries as discussed in Grill et al. (2014). The inner crust EoS has been published in Fortin et al. (2016).

3. Mixed System of Two Components

We assume no interaction between DM and BM, except through gravity. This assumption is fully justified by the latest constraints coming from the DM direct detection experiments and Bullet Cluster (Clowe et al. 2006; Randall et al. 2008), showing that the DM-BM cross section is many orders of magnitude lower than the typical nuclear one, $\sigma_\chi \sim 10^{-45}\,{\rm cm}^2 \ll \sigma_N \sim 10^{-24}\,{\rm cm}^2$.

Therefore, the stress-energy tensors of both components are conserved separately, leading to the system of the TOV equations with split components (Oppenheimer & Volkoff 1939; Tolman 1939)

$$\frac{dp_i}{dr} = -\frac{(\epsilon_i + p_i)(M_{\rm tot} + 4\pi r^3 p_{\rm tot})}{r^2(1 - 2M_{\rm tot}/r)}, \tag{7}$$

which describes the relativistic hydrostatic equilibrium of a DM-admixed NS. In Equation (7), the subscript index refers both to the BM and DM, i.e., $i = B, D$, while $p_{\rm tot} \equiv p_B + p_\chi$ and $M(r)$ are the total pressure and gravitational mass enclosed inside a sphere of radius r, respectively,

$$M_i(r) = 4\pi \int_0^r \varepsilon_i(r') r'^2 dr'. \tag{8}$$

Using Equation (8), we define the total gravitational mass as the sum of the two components, $M_{\rm tot} = M_B(R_B) + M_D(R_D)$, where the radii R_i are evaluated using the zero-pressure condition at the surface

$$p_i(R_i) = 0. \tag{9}$$

After having the total mass of the system, it is possible and convenient to write the fraction of the accumulated DM as

$$f_\chi = \frac{M_D}{M_{\rm tot}}. \tag{10}$$

It is worth noting, that we refer to the microscopic/thermodynamic DM parameters as χ, while the macroscopic ones have an index D.

It is easy to obtain directly from Equation (7) the relation between the chemical potentials of the BM and DM. In fact, Ivanytskyi et al. (2020) showed that

$$\frac{d\ln \mu_B}{dr} = \frac{d\ln \mu_\chi}{dr} = -\frac{M_{\rm tot} + 4\pi r^3 p_{\rm tot}}{r^2(1 - 2M_{\rm tot}/r)}, \tag{11}$$

which yields the conclusion that the two chemical potentials are proportional to each other. The value their ratio attains in the center of the star is the proportionality constant, which can be used to simplify the model

$$\mu_\chi = \left(\frac{\mu_\chi}{\mu_B}\right)_{r=0} \mu_B. \tag{12}$$

By solving the TOV Equation (7) with the boundary conditions and accounting for the relation between both components from Equation (12), we calculate the M-R relations for DM-admixed NSs for different values of DM fractions f_χ, particle's mass m_χ, and the interaction scale m_I. To better understand the impact of each parameter we consider light and heavy DM particles with $m_\chi = 100$ MeV and $m_\chi = 1000$ MeV (see the left column of Figure 2). Moreover, to address our ignorance of the EoS for baryonic component we studied the effect of DM on the soft IST EoS, depicted as a solid black curve on the left panels of Figure 2, as well as on the stiff DD2Λ EoS (dotted black curve) and DD2 EoS (dashed–dotted black curve). The chosen EoSs represent different sides of mass and radius region allowed by the recent astrophysical, GW, and nuclear physics constraints, and therefore, provide good coverage of BM parameters. As it can be seen, the DD2Λ EoS (dotted black curve) and DD2 EoS coincide until $\sim$1.4 $M_\odot$, a point where the onset of hyperons happens. Further, hyperon production softens the EoS leading to a smaller total maximum mass and star's radius.

The left panels of Figure 2 show the effect of DM with different relative fractions inside a star on its mass and radius. Thus, we see a reduction of $M_{\rm max}$ and radius of stars for larger DM fractions caused by a DM core formation. In fact, the formation of more compact objects for an outside observer would look like a softening of the BM EoS. This degeneracy between the effect of DM and possible change of the strongly interacting matter properties at high density will be discussed in Section 6.

Due to the fact that in the considered model at $\mu_\chi \to \sqrt{2} m_\chi$ energy density diverges at finite pressure, DM falls under the Schwarzschild radius forming a black hole. It takes place for the high-mass stars for which the DM chemical potential in the center reaches the limit (see the upper left panel of Figure 2).

The panels on the middle and right columns of Figure 2 demonstrate the split energy density profiles of DM (dashed curves) and BM (dotted curves). The solid black curve depicts the energy density profile for the 1.4 $M_\odot$ star. The profiles for DM-admixed NSs are shown for stars with the same total gravitational mass as the pure BM NS. As the onset of

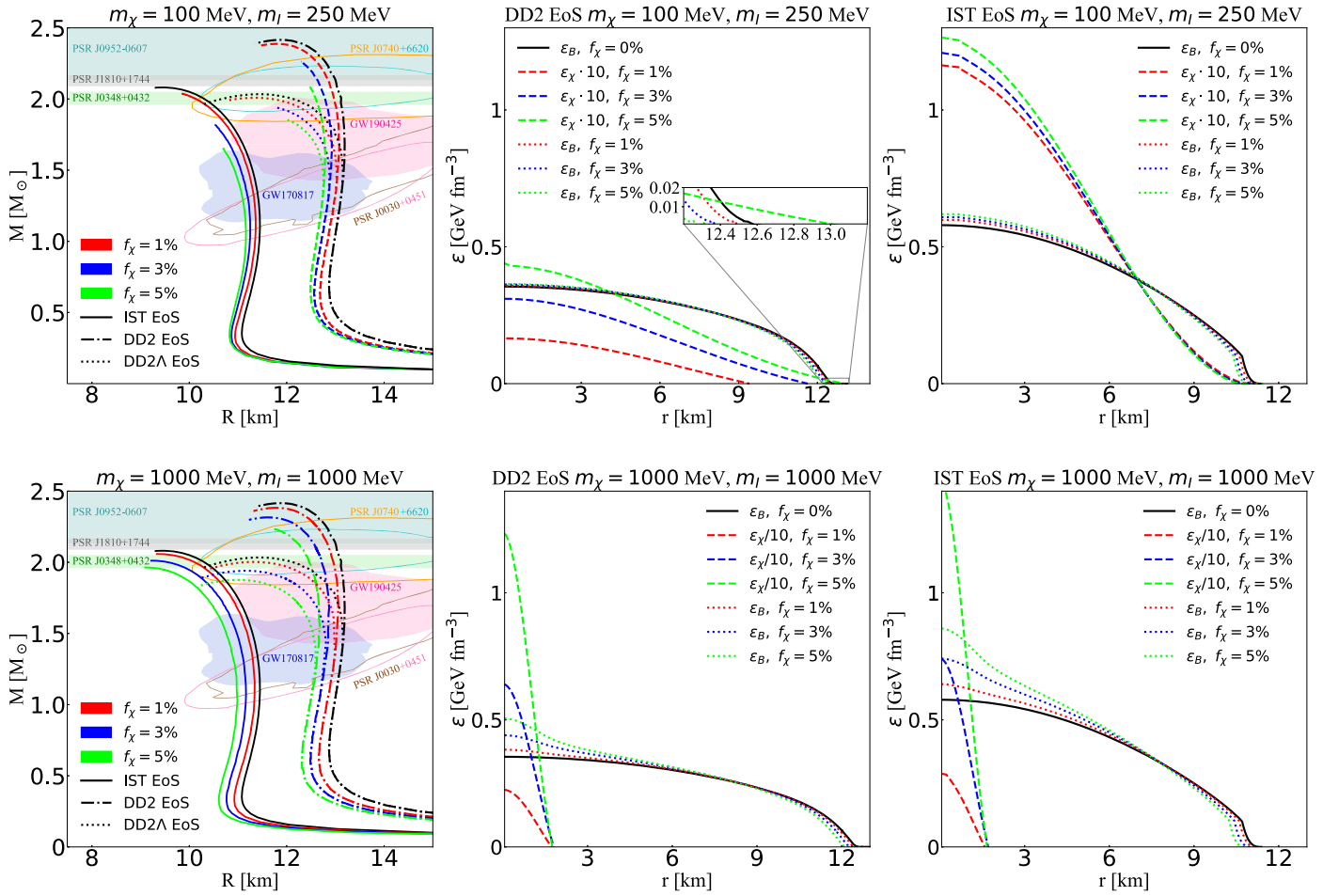

Figure 2. Left column: total gravitational mass of the DM-admixed NS as a function of its visible radius R obtained for $m_\chi = 100$ MeV, $m_I = 250$ MeV (upper panel), and $m_\chi = 1000$ MeV, $m_I = 1000$ MeV (lower panel). Black solid, dashed–dotted, and dotted curves correspond to pure BM stars described by the IST EoS, DD2 EoS, and DD2 EoS with hyperons. Red, blue, and green colors depict relative DM fractions equal to 1%, 3%, and 5%, correspondingly. Green, gray, and teal bands represent 1σ constraints on mass of PSR J0348+0432 (Antoniadis et al. 2013), PSR J1810+1744 (Romani et al. 2021), and PSR J0952-0607 (Romani et al. 2022). Pink and beige contours show the NICER measurements of PSR J0030+0451 (Miller et al. 2019; Riley et al. 2019), while orange and blue contours depict the PSR J0740+6620 measurements (Miller et al. 2021; Riley et al. 2021). LIGO-Virgo observations of GW170817 (Abbott et al. 2018) and GW190425 (Abbott et al. 2020a) binary NS mergers are shown in blue and magenta. Middle column: energy density profiles for the BM (dotted curves) and DM (dashed curves) components are shown for the DD2 EoS. The solid black curve represents the profile for pure BM 1.4 $M_\odot$ NS, while the other profiles were sampled to have the same total gravitational mass. The upper panel is obtained for $m_\chi = 100$ MeV, $m_I = 250$ MeV and the lower one for $m_\chi = 1000$ MeV, $m_I = 1000$ MeV. Right column: the same as on the middle column, but for the IST EoS.

hyperons occurs after 1.4 $M_\odot$, two formulations of the DD2 EoS give the same prediction for the matter distribution inside the stars. Therefore, in Figure 2 we show profiles only for the DD2 EoS.

For heavy bosons a compact DM core is formed, which is seen from the high values of the ϵ_D, being an order of magnitude above ϵ_B (see the middle and right panels of the low row in Figure 2). Furthermore, the ϵ_D drops to zero at radius $\sim$2 km corresponding to the size of a DM core.

For the DM fraction 5% and $m_\chi = 100$ MeV, $m_I = 250$ MeV (see the middle upper panel of Figure 2) a DM halo is formed with the radius of 13.0 km.

4. Tidal Deformability of DM-admixed NSs

The tidal deformability parameter λ quantifies the response of an object to a static external quadrupolar tidal field $\mathcal{E}_{ij}$ by relating it to a quadrupolar moment $\mathcal{Q}_{ij} = -\lambda \mathcal{E}_{ij}$. For a given stellar configuration of the total mass $M_{\rm tot}$ and radius R this tidal deformability can be expressed through the Love number k_2 as $\lambda = 2k_2R^5/3$ and is commonly mapped to the dimensionless $\Lambda = \lambda/M_{\rm tot}^5$ (Hinderer 2008). In the two-component case, R should be understood as the outermost radius, i.e., $R = R_B$ in the DM core scenario and $R = R_D$ in the DM halo one. The Love number is defined through the solution of an ordinary differential equation (ODE) appearing as a leading order expansion of the Einstein equations with a metric perturbed by the external gravitational field (Regge & Wheeler 1957). The microscopic properties of matter are encoded into this ODE through the change of total pressure $p_{\rm tot} \equiv p_B + p_\chi$ caused by perturbation of the total energy density $\varepsilon_{\rm tot} \equiv \varepsilon_B + \varepsilon_\chi$. This change is quantified by the derivative $dp_{\rm tot}/d\varepsilon_{\rm tot}$. In the barotropic one-fluid case, this derivative represents the corresponding speed of sound. In the two-fluid case, the speed of sound derivation as $dp_{\rm tot}/d\varepsilon_{\rm tot}$ is mathematically identical to the expression obtained by Das et al. (2020a). Therefore, in what follows, we refer to it as the effective speed of sound of the two-fluid system. It can be expressed through the speed of

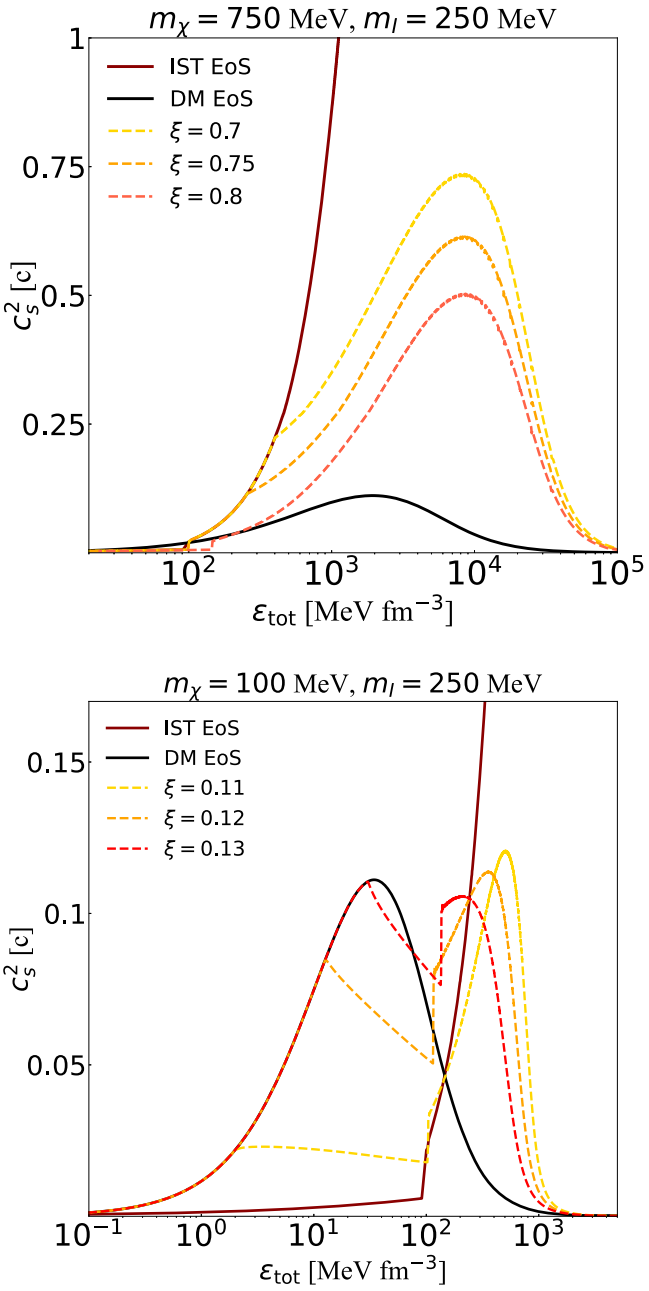

Figure 3. The effective speed of sound for a mixture of BM and DM as a function of total energy density. Upper panel: the curves were obtained for $m_\chi = 750$ MeV and $m_I = 250$ MeV, which represents a DM core configuration. Lower panel: the same as on the upper panel, but for $m_\chi = 100$ MeV and $m_I = 250$ MeV illustrating a DM halo configuration. The horizontal line at low densities corresponds to the polytropic EoS for the crust.

sound of baryonic $c^2_{s,B}$ and dark $c^2_{s,\chi}$ components as

$$c^2_{s,\rm eff} = \eta c^2_{\rm s,B} + (1 - \eta) c^2_{s,\chi} \tag{13}$$

with $\eta \in [0, 1]$. The lower and upper edges of this interval correspond to the cases of pure DM and BM, respectively. Appendix B provides the derivation of Equation (13) and parameter η. This expression demonstrates that the effective speed of sound lies between the ones of pure components.

In Figure 3 we show the effective speed of sound for different $\xi = \frac{\mu_\chi}{\mu_B}$ values, as well as the speed of sound for pure BM and DM components. A relation between the parameters ξ and η is given in Equation (B3) in Appendix B. The upper panel of Figure 3 indicates how the effective speed of sound behaves with DM accumulated in a core of a compact star. Note, that it is in between the speed of sound values for pure components. On the lower panel of Figure 3, we see that the effective speed of sound follows the BM, and only in the outer crust the DM component stars dominate, which is related to a halo configuration.

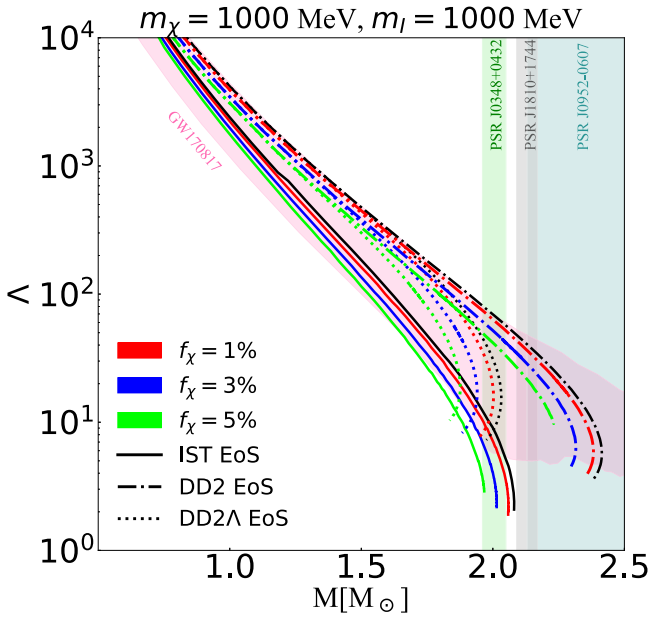

Figure 4. Tidal deformability as a function of total gravitational mass calculated for pure BM stars (black curves) and DM-admixed NSs with relative DM fractions 1%, 3%, and 5%, in red, blue, and green, correspondingly. Solid, dashed–dotted and dotted curves represent the IST EoS, DD2 EoS, and DD2Λ EoS. The colors and symbols coincide with the ones used in Figure 2 for a better comparison. The figure is obtained for $m_\chi = 1000$ MeV, $m_I = 1000$ MeV. Green, gray, and teal bands represent 1σ constraints on mass of PSR J0348+0432 (Antoniadis et al. 2013), PSR J1810+1744 (Romani et al. 2021), and PSR J0952-0607 (Romani et al. 2022). The magenta area visualizes the constraints obtained from GW170817 (Abbott et al. 2018).

As can be seen in Figure 4, for the given total gravitational mass DM condensed in a core leads to a smaller tidal deformability parameter compared to a pure baryonic star. A similar effect has been shown in Figure 2 for the radius. For a distant observer, these effects will be perceived as an effective softening of the EoS. On the other hand, the presence of a DM halo leads to a significant increase in the outermost radius that goes beyond the BM component, an increase of the tidal deformability parameter, and consequent effective stiffening of the EoS. The considered IST, DD2, and DD2Λ EoSs make us conclude that the soft EoS, being on the lower limit of the GW170817 90% CL region (see the magenta area in Figure 4), provides a stringent constraint on a DM core scenario, while the stiff EoS, being on the upper border of it, allows much higher DM fractions, and disfavors an extended halo configuration. This degeneracy between the effect of DM and strongly interacting matter properties at high densities possesses limitations on DM detection, except for several DM smoking guns that are going to be discussed in Section 6. Despite it, we have to be aware of the fact that observational data on compact stars could be affected by accumulated DM, and consequently, constraints we put on strongly interacting matter at high densities.

5. Results

To study an interplay between boson mass and the interaction scale, as well as to put constraints on the DM fraction, we perform a scan over those parameters for the IST EoS (upper row), DD2 EoS (middle row), and DD2Λ EoS (bottom row) for fixed DM fractions of 1%, 3%, and 5% (see Figure 5 in Appendix C). The color maps represent the total maximum gravitational mass of DM-admixed NSs. The white curve on each panel corresponds to $M_{\rm max} = 1.4\,M_{\odot}$, whereas the red curve represents $M_{\rm max} = 2.0\,M_{\odot}$. In the case $2.0\,M_{\odot}$ configurations are not reachable, we indicate $1.9\,M_{\odot}$ stars with a green curve. As one can see from the upper row in Figure 5, the increase of the DM fraction narrows the range of the values of the interaction scale m_I consistent with the masses of the heaviest known pulsars. On the other hand, the existence of the high-mass stars with a significant amount of heavy DM requires low values of the interaction scale.

We see the same dependence between m_χ and m_I values. In fact, lower $m_I \equiv m_\omega/g$ values correspond to the higher coupling constant g or, equivalently, stronger repulsion between the DM particles. The IST EoS for any DM fraction is always in agreement with the tidal deformability constraint, independently of m_χ and m_I (see the upper row in Figure 5). At the same time, only for 1% and 3% of DM the total maximum mass of DM-admixed NSs can reach $2.0\,M_{\odot}$. Thus, to simultaneously reproduce $2.0\,M_{\odot}$ and GW170817 tidal deformability constraints the boson mass and interaction scale are restricted to the values shown in yellow. The shaded areas correspond to the non-allowed regions of parameters that cannot simultaneously provide the heaviest pulsars and GW constraints.

For 3% and 5% of DM the DD2 EoS reproduces both constraints in a wide range of parameters disfavoring megaelectronvolt mass range of bosonic DM with low values of the interaction strength. The black curve in the middle and bottom rows of Figure 5 depicts the GW170817 tidal deformability constraint $\tilde{\Lambda}_{1.36} = 720$ (Abbott et al. 2019b) above which the model is consistent with the GW170817 merger. The dashed area corresponds to a non-allowed range of parameters, including 1% of DM for the DD2 EoS. For the DD2Λ EoSs there are no m_I and m_χ values that simultaneously reproduce the heaviest pulsars and GW constraints. In fact, only one of these criteria was reproduced for considered values of DM fractions. This is directly related to the fact that at the onset of Λ hyperons the EoS becomes softer in addition to the DM softening effect in a core configuration.

From this analysis, we can conclude that, contrary to the stiff BM EoS (the DD2 EoS, as an example), the soft BM EoS (the IST EoS, as an example) provides a weaker limit on DM particle mass and interaction strength. This is related to the fact that the pure baryonic DD2 or DD2Λ EoSs are on the upper border of the $\Lambda_{1.4}$ constraint from GW170817. Any decrease in $\Lambda_{1.4}$ due to a DM core will not violate this condition, whereas a small DM halo configuration will do it. As can be seen in Figure 4, the IST EoS is located on the lower limit of the magenta area favoring a halo formation.

It is worth noting that this result is obtained under the assumption of a similar DM fraction in all galaxies. As a matter of fact, an application of the GW170817 tidal deformability result and multi-messenger data as a universal constraint on the amount of DM is questionable. Each galaxy could be characterized by a different DM profile, as well as have local DM inhomogeneities. Strictly speaking, GW170817 probes an amount of DM only in a part of the NGC 4993, the host galaxy for this particular merger. Therefore, a larger sample size of NS–NS and NS–BH mergers is required to constrain the DM properties.

Due to current uncertainties of the BM EoS at high density, we cannot discriminate between the effect of DM and the properties of BM. As it will be discussed in the following Section 6, we expect a higher DM fraction inside compact stars toward the Galactic Center. If so, the compact star population would follow the scenarios presented from the left to right panels in Figure 5, i.e., from low to high DM fraction.

6. Discussions

As described above, there are various effects of DM on compact stars. A natural question arises: how we can narrow down the proposed DM models and constrain the DM properties using NSs? Can compact stars provide a smoking gun evidence for the presence of DM? There are several different approaches:

(i) By measuring the mass, radius, and moment of inertia of NSs with few-percent accuracy. Nowadays, NICER (Miller et al. 2019, 2021; Raaijmakers et al. 2020, 2021) and in the near future ATHENA (Cassano et al. 2018), eXTP (in't Zand et al. 2019), and STROBE-X (Ray et al. 2019) are expected to measure M and R of NSs with a high accuracy. Using the synthetic data for the STROBE-X telescope, and assuming two NSs of the same mass and BM EoS, Rutherford et al. (2022) concluded that a measurement of radii with a 2% accuracy would be enough to draw a conclusion about the presence of DM in star's interior. However, the existence of the deconfinement phase transition in a core would exhibit in the same way, leading to a degeneracy between the effect of DM and the phase transition. The main drawback of this approach is that the effect of DM could mimic the softening/stiffening of BM at high density and vice versa. Current uncertainties of the baryonic EoS do not allow discrimination of two effects. In addition, radio telescopes, e.g., MeerKAT (Bailes et al. 2018), SKA (Watts et al. 2015), and ngVLA (Bower et al. 2018) plan to increase radio pulsar timing and discover Galactic Center pulsars. A mass reduction of NSs toward the Galactic Center or variation of mass, radius, and moment of inertia in different parts of the Galaxy could shed light on the amount of accumulated DM in compact stars. In fact, we could see a paucity of old millisecond pulsars in the Galactic Center either due to light extinction on dust, or the collapse of DM-admixed NSs into black holes after exceeding the Schwarzschild limit (Bramante & Linden 2014).

(ii) By performing binary numerical-relativity simulations and kilonova ejecta for DM-admixed compact stars for different DM candidates, mass of particles, interaction strength, and fractions with the further comparison to GW and electromagnetic signals. The smoking gun of the presence of DM could be a supplementary peak in the characteristic GW spectrum of NS mergers (Ellis et al. 2018a), exotic waveforms (Giudice et al. 2016), modification of the kilonova ejecta, or the presence of a strong oscillation mode in the waveforms during the post-merger stage (Bezares et al. 2019). The next generation of GW

detectors, i.e., the Cosmic Explorer (Mills et al. 2018) and Einstein Telescope (Punturo et al. 2010) will open another perspective of detection of post-merger regimes and probing an internal composition of compact stars.

(iii) By detecting a new feature in the binary Love relation (Yagi & Yunes 2016). Thus, as it was shown in Figure 3, DM could produce a bump, or any other irregular behavior, in the effective speed of sound that would affect the binary Love relation. Similar, as it was demonstrated for the strongly interacting matter by Tan et al. (2022). This mark may be revealed by the next generation of GW detectors that are planned to have the measurement precision of $\delta\Lambda \sim 5$ for a GW170817-like event.

(iv) By detecting objects that go in contradiction with our understanding. A potential candidate for DM-admixed NS could be the secondary component of GW190814 (Abbott et al. 2020b). While likely being a black hole (Essick & Landry 2020; Tews et al. 2021), this compact object with the mass of $\sim 2.6\,M_{\odot}$ raised debates about its nature (Tsokaros et al. 2020) as a pure BM EoS would not be able to explain a compact star of $\sim 2.6\,M_{\odot}$. Hence, if not being a black hole, the compact object would have to be supplemented either with exotic degrees of freedom, such as hyperons and/or quarks (Tan et al. 2020; Dexheimer et al. 2021), an early deconfinement phase transition (Ivanytskyi & Blaschke 2022), very fast rotation (Zhang & Li 2020), or extra stiffening of the EoS at high densities (Fattoyev et al. 2020). An alternative explanation of this puzzle would be a DM-admixed NS (Di Giovanni et al. 2022), which could also explain a formation of a black hole of so low mass as a collapsed DM-admixed NS (Bramante & Linden 2014).

The recently announced measurement of the central compact object within the supernova remnant HESS J1731-347 (Doroshenko et al. 2022) is another object that puzzles our understanding. This lightest and smallest compact star ever observed could be explained as an NS admixed with DM (Sagun et al. 2023).

(v) Modification of the pulsar pulse profile due to the extra light-bending (Miao et al. 2022) and/or gravitational microlensing in the case of the existence of a dark halo.

(vi) Modification of the cooling rate of compact stars (de Lavallaz & Fairbairn 2010; Hamaguchi et al. 2019; Ángeles Pérez-García et al. 2022; Buschmann et al. 2022). We want to note, that this effect is the most inaccurate among the abovementioned ones. Thus, NSs need to have a well-measured surface luminosity and age. In addition to it, uncertainties related to particle composition, EoS, magnetic field, superfluidity/superconductivity, NS masses, the chemical composition of an atmosphere, etc., could wash out an effect of DM. Old NSs are less affected by the mentioned effects, as a photon cooling stage starts to dominate over a neutrino cooling stage that is very sensitive to a particle composition and superfluidity/superconductivity (Page et al. 2004). The magnetic field is also expected to be unimportant for old isolated NSs. Therefore, a possible heating mechanism of NSs due to DM annihilation could be probed by increasing statistics on observational data of old NSs.

7. Conclusions

We proposed a model of bosonic DM represented by a complex scalar field coupled to the vector one through the covariant derivative, which is equivalent to scalar electrodynamics with massive photons. The model describes DM existing in the form of BEC with repulsive interaction. Pressure of the present EoS saturates at asymptotically high densities leading to the vanishing speed of sound and compressibility at this regime. From the thermodynamic requirements, the chemical potential of DM existing as such BEC is limited to the interval $\mu_{\chi} \in [m_{\chi}, \sqrt{2}m_{\chi}]$, with m_{χ} being the DM particle mass. In the weak and strong coupling limits, this interval shrinks to its lower and upper bounds, respectively, while pressure vanishes even at any density. This spectacular feature of the present model makes its weak and strong coupling limits qualitatively similar and requires further clarification.

At the same time, the strong coupling limit is shown to be inconsistent with the Bullet Cluster cosmological data. Confronting the model prediction on the cross section of the DM self-interaction to the results of numerical simulations and observations allowed us to constrain the interaction scale m_I from below depending on the DM particle mass m_{χ}.

DM-admixed compact stars were modeled by considering the mixed system of two fluids with different relative fractions. The performed derivation of the effective speed of sound for a two-fluid system allowed us to calculate the tidal deformability parameter for compact stars admixed with different amounts of DM. We argue that the one-fluid approach cannot be applied to a mixed system of several components with the different proper speed of sound values.

To account for a discrepancy related to the baryonic component the soft IST EoS and stiffer DD2 EoS with and without hyperons were considered. For different DM particle's mass, its relative fraction, and interaction scale we found the conditions of DM core formation. We argue that in the framework of the considered model only a small DM halo is possible, with the outermost radius around twice the baryonic one. However, the total maximum gravitational mass of this configuration is below $2\,M_{\odot}$.

We performed a thorough analysis of the effect of DM particle mass in the 100–1000 MeV mass range and self-interacting scale on maximum total gravitational mass and tidal deformabilities of NSs for several fixed DM fractions. We found that for 1%, 3% of DM for the IST EoS and 3%, 5% of DM for the DD2 EoS the model can simultaneously reproduce the heaviest pulsars and GW170817 tidal deformability constraint. The obtained allowed region of boson mass m_{χ} and interaction scale m_I for a fixed DM fraction shows an anticorrelated dependence between these parameters, i.e., a high m_{χ} value favors a low m_I value. For the DD2Λ EoS no allowed region of parameters was found due to the inability to simultaneously reproduce both constraints.

The considered DM fractions up to 5% were chosen to demonstrate the effects on compact star properties, and as was discussed in the Introduction, are higher than could be accumulated by Bondi accretion. While up-to-date calculations are based on the interaction between DM and BM, the self-interaction of DM could lead to enhanced DM accretion, hence the DM fraction here proposed. However, we leave this for future studies.

In Section 6, we discussed the possible smoking gun signatures of DM in compact stars that could be probed in the near future, e.g., alteration of maximum total gravitational mass and radius of compact stars as a function of a distance from the Galactic Center; modification of the surface temperature (an additional heating or cooling mechanism) of NSs toward the Galactic Center; lack of old millisecond pulsars in the Galactic Center; the presence of supplementary peak(s) in the GW signal from NS–NS and/or NS–BH mergers, exotic waveform, or modification of the kilonova ejecta; gravitational-lensing effect or alteration of the pulsar pulse profile due to the extra light bending in a dark halo. Moreover, such objects as a secondary component of the GW190814 event and central compact object within the supernova remnant HESS J1731-347 challenge the existing models of compact stars and black holes, offering the possibility of these objects being a DM-admixed NS.

We argue that compact stars and their mergers provide a novel sensitive indirect method of detection and constraining the DM properties. Based on the performed analysis it is clear that the present data analysis of X-ray, radio, and GW observations without accounting for an accumulated DM could miss a valuable piece of information as well as give an incorrect prediction about the strongly interacting matter properties at high density.

Acknowledgments

The work of E.G., C.P., and V.S. was supported by national funds from FCT—Fundação para a Ciência e a Tecnologia, I. P., within project Nos. UIDB/04564/2020, UIDP/04564/2020, and EXPL/FIS-AST/0735/2021. E.G. also acknowledges the support from project No. PRT/BD/152267/2021. C. P. is supported by the project No. PTDC/FIS-AST/28920/2017. V.S. also acknowledges the PHAROS COST Action CA16214. The work of O.I. was supported by the program Excellence Initiative–Research University of the University of Wrocław of the Ministry of Education and Science.

Appendix A
Lagrangian Model of the DM EOS

Here, we derive the DM EoS, presented with Equations (1) and (2), and we analyze it in the weak and strong coupling regimes. The minimal Lagrangian describing the chosen model of DM should include mass and kinetic terms of the complex scalar χ and real vector ω^μ fields, which are coupled through the covariant derivative $D^\mu = \partial^\mu - ig\omega^\mu$ with g being the corresponding Yukawa coupling constant. Thus, we start with

$$\mathcal{L} = (D_\mu\chi)^* D^\mu\chi - m_\chi^2\chi^*\chi - \frac{\Omega_{\mu\nu}\Omega^{\mu\nu}}{4} + \frac{m_\omega^2\omega_\mu\omega^\mu}{2}, \quad \text{(A1)}$$

where m_χ and m_ω are masses of the scalar and vector fields, respectively, and $\Omega_{\mu\nu} = \partial_\mu\omega_\nu - \partial_\nu\omega_\mu$. Before going further we would like to discuss the Neother current resulting from the Lagrangian (A1)

$$j^\mu = i\left[\chi^*\frac{\partial\mathcal{L}}{\partial(\partial_\mu\chi^*)} - \chi\frac{\partial\mathcal{L}}{\partial(\partial_\mu\chi)}\right] = i[\chi^* D^\mu\chi - \chi(D^\mu\chi)^*] = i(\chi^*\partial^\mu\chi - \chi\partial^\mu\chi^*) + 2g\omega^\mu\chi^*\chi. \quad \text{(A2)}$$

This current is equivalent to the one corresponding to local $U(1)$ symmetry of $\mathcal{L}$ (Brading & Brown 2000). The density of conserved charge associated to the DM particles is obtained by averaging the zeroth component of this current. The second term in the expression for j^μ vanishes under such averaging, since it includes an odd number of creation and annihilation operators of the vector field. Thus, $n_\chi = \langle j^0\rangle = i\langle\chi^*\partial^0\chi - \chi\partial^0\chi^*\rangle$. This relation is artificially violated in the case when ω^μ is treated classically, e.g., within the mean-field approximation. This discrepancy can be removed by using the Noether current resulting from the invariance with respect to global $U(1)$ transformation (Brading & Brown 2000)

$$j^\mu = i(\chi^*\partial^\mu\chi - \chi\partial^\mu\chi^*). \quad \text{(A3)}$$

Below we use this expression for the DM four current.

Within the mean-field approximation operator of the vector field in this Lagrangian is replaced by its constant expectation value. This value can be obtained from the corresponding Euler–Lagrange equation

$$(\partial^2 + m_\omega^2 + 2g^2\chi^*\chi)\omega^\mu - \partial^\mu\partial^\nu\omega_\nu + gj^\mu = 0. \quad \text{(A4)}$$

In the hydrostatic case only the zeroth component of the DM four-current attains nonzero mean value being nothing else as the DM particle number density n_χ, i.e., $\langle j^\mu\rangle = \eta^{\mu 0} n_\chi$ with $\eta^{\mu\nu}$ standing for the Minkowski metric tensor. Replacing ω^μ by its constant mean value we eliminate derivatives of the vector field in Equation (A4). Furthermore, we replace $\chi^*\chi$ by the scalar field condensate $\langle\chi^*\chi\rangle$ and DM current by its mean value. Thus, the Euler–Lagrange equation of the vector field under the mean-field approximation can be given a form of

$$\langle\omega^\mu\rangle = \eta^{\mu 0}\omega \quad \text{with} \quad \omega = -\frac{gn_\chi}{m_\omega^2 + 2g^2\langle\chi^*\chi\rangle}. \quad \text{(A5)}$$

At finite particle number densities, DM has finite chemical potentials μ_χ, which serves as a Lagrange multiplier in $\mathcal{L} + \mu_\chi j^0$ ensuring that mean value of j^0 coincides with n_χ. Inserting Equation (A5) into Equation (A1), one gets

$$\mathcal{L} + \mu_\chi j^0 = \partial_\mu\chi^*\partial^\mu\chi - M_\chi^2\chi^*\chi + \nu_\chi j^0 + \frac{m_\omega^2\omega^2}{2}. \quad \text{(A6)}$$

The first three terms on the right-hand side of this equation represent free quasi-particles with the effective mass and chemical potential defined as

$$M_\chi^2 \equiv m_\chi^2 - g^2\omega^2, \quad \text{(A7)}$$

$$\nu_\chi \equiv \mu_\chi + g\omega, \quad \text{(A8)}$$

respectively. At zero temperature these bosonic quasi-particles condense to zero mode with $\langle\chi^*\chi\rangle = \zeta^2$ and ζ being an amplitude of this mode. This BEC contributes to the DM pressure $\zeta^2(\nu_\chi^2 - M_\chi^2)$ (see, e.g., chapter 2.4 of Kapusta & Gale 2006). The last term in Equation (A6) does not include

any dynamical variables, and therefore, simply renormalizes the pressure, which becomes

$$p_\chi = \zeta^2(\nu_\chi^2 - M_\chi^2) + \frac{m_\omega^2\omega^2}{2}. \tag{A9}$$

Mean value of the vector field defined by Equation (A4) maximizes the pressure. The same is the case for ζ, i.e., $\frac{\partial p_\chi}{\partial \omega} = \frac{\partial p_\chi}{\partial \zeta} = 0$. These conditions should be supplemented with a definition of the DM particle number density given by the thermodynamic identity $n_\chi = \frac{\partial p_\chi}{\partial \mu_\chi}$ yielding the following system of equations, which should be solved in order to find ω and ζ and construct the DM EoS:

$$2g\zeta^2(\nu_\chi + g\omega) + m_\omega^2\omega = 0, \tag{A10}$$

$$2\zeta(\nu_\chi^2 - M_\chi^2) = 0, \tag{A11}$$

$$n_\chi = 2\zeta^2\nu_\chi. \tag{A12}$$

Before solving this system, we want to demonstrate that it is consistent with Equation (A5). For this we formally express ν_χ from Equation (A12) and insert the result to Equation (A10) yielding $gn_\chi + (2g^2\zeta^2 + m_\omega^2)\omega = 0$. Then, replacing ζ^2 by $\langle\chi^*\chi\rangle$ this relation can be written in the desired form.

In the BEC, amplitude of the bosonic zero mode is $\zeta \neq 0$. Therefore, Equation (A11) requires $\nu_\chi = M_\chi$, which can be solved with respect to the vector field as

$$\omega = \frac{-\mu_\chi \pm \sqrt{2m_\chi^2 - \mu_\chi^2}}{2g}. \tag{A13}$$

the DM particle number density we first express ζ^2 from Equation (A10) and then insert the result into Equation (A12). Thus, at $\mu_\chi \in [m_\chi, \sqrt{2}m_\chi]$ the DM EoS becomes

$$p_\chi = \frac{1}{4}\left(\frac{m_\omega}{g}\right)^2(m_\chi^2 - \mu_\chi\sqrt{2m_\chi^2 - \mu_\chi^2}), \tag{A14}$$

$$n_\chi = \frac{1}{2}\left(\frac{m_\omega}{g}\right)^2\frac{\mu_\chi^2 - m_\chi^2}{\sqrt{2m_\chi^2 - \mu_\chi^2}}, \tag{A15}$$

while at $\mu_\chi \in [0, m_\chi]$ one gets $p_\chi = 0$ and $n_\chi = 0$. It is seen from these expressions that vector field mass m_ω and coupling g do not enter the DM EoS independently but appear as the ratio $m_I \equiv m_\omega/g$, which is a relevant parameter. With this notation and thermodynamic identity $\varepsilon_\chi = \mu_\chi n_\chi - p_\chi$, we arrive at Equations (1) and (2).

The weak and strong coupling limits of the present EoS are obtained at $g \to 0$ and $g \to \infty$, respectively. This corresponds to $m_I \to \infty$ and $m_I \to 0$. In order to consider these limits we treat the DM particle density as an independent quantity. For this we first write Equation (A15) as a quadratic equation for $\sqrt{2m_\chi^2 - \mu_\chi^2}$ and solve it as

$$\sqrt{2m_\chi^2 - \mu_\chi^2} = \sqrt{m_\chi^2 + \frac{n_\chi^2}{m_I^4}} - \frac{n_\chi}{m_I^2}. \tag{A16}$$

This solution allows us to express μ_χ and expand it up to the leading order in m_I^{-2} or m_I^2

$$\mu_\chi = \begin{cases} m_\chi + \dfrac{n_\chi}{m_I^2} + \mathcal{O}(m_I^{-4}), & m_I \to \infty \\ \sqrt{2}\,m_\chi - \dfrac{m_\chi^3 m_I^4}{8\sqrt{2}n_\chi^2} + \mathcal{O}(m_I^8), & m_I \to 0. \end{cases} \tag{A17}$$

From this condition we immediately conclude that physical values of the DM chemical potential are limited to the range $-\sqrt{2}m_\chi \leqslant \mu_\chi \leqslant \sqrt{2}m_\chi$. At positive μ_χ BEC is constituted by the DM particles, while negative μ_χ corresponds to antiparticles. For definiteness in this work, we consider the case of the

From this we conclude that in the weak coupling limit chemical potential of DM converges to the smallest value of the BEC interval $\mu_\chi \in [m_\chi, \sqrt{2}m_\chi]$, while in the strong coupling limit it converges to the largest value. This conclusion holds for any n_χ. The DM pressure behaves as

$$p_\chi = \frac{m_I^2}{8}(\mu_\chi - \sqrt{2m_\chi^2 - \mu_\chi^2})^2 = \begin{cases} \dfrac{n_\chi^2}{2m_I^2} + \mathcal{O}(m_I^{-4}), & m_I \to \infty \\ \dfrac{m_\chi^2 m_I^2}{4} + \mathcal{O}(m_I^4), & m_I \to 0 \end{cases}, \tag{A18}$$

DM particles, which is equivalent to requiring $\mu_\chi \geqslant 0$. Equation (A13) ensures that the first term in Equation (A9) vanishes and DM pressure $p_\chi \propto \omega^2$. At zero n_χ this pressure should vanish provided by $\omega = 0$. At non-negative chemical potential of DM this condition can be fulfilled only at $\mu_\chi = m_\chi$ if the sign "+" is chosen in Equation (A13). In order to obtain

where on the second step $\sqrt{2m_\chi^2 - \mu_\chi^2}$ was approximated by $m_\chi - n_\chi/m_I^2$ at $m_I \to \infty$, while at $m_I \to 0$ it was neglected compared to μ_χ. In both of the considered limits the pressure vanishes leading to the energy density mentioned in Section 2.1.

Appendix B
Effective Speed of Sound of Two-fluid System

In order to calculate $c^2_{s,\chi}$ we notice that in the GCE pressure and energy density of each component are functions of the corresponding chemical potential. With this we can write

$$c^2_{s,\mathrm{tot}} = \frac{dp_{\mathrm{tot}}}{d\varepsilon_{\mathrm{tot}}} = \frac{\frac{\partial p_B}{\partial \mu_B} + \frac{\partial p_\chi}{\partial \mu_\chi}\frac{d\mu_\chi}{d\mu_B}}{\frac{\partial \varepsilon_B}{\partial \mu_B} + \frac{\partial \varepsilon_\chi}{\partial \mu_\chi}\frac{d\mu_\chi}{d\mu_B}} = \frac{\frac{\partial \varepsilon_B}{\partial \mu_B}c^2_{s,B} + \frac{\partial \varepsilon_\chi}{\partial \mu_\chi}\frac{d\mu_\chi}{d\mu_B}c^2_{s,\chi}}{\frac{\partial \varepsilon_B}{\partial \mu_B} + \frac{\partial \varepsilon_\chi}{\partial \mu_\chi}\frac{d\mu_\chi}{d\mu_B}}, \quad \text{(B1)}$$

where on the last step we used identities $c^2_{s,B} = \frac{\partial p_B}{\partial \mu_B}/\frac{\partial \varepsilon_B}{\partial \mu_B}$ and $c^2_{s,\chi} = \frac{\partial p_\chi}{\partial \mu_\chi}/\frac{\partial \varepsilon_\chi}{\partial \mu_\chi}$ in order to express derivatives of the pressures of two components with respect to the corresponding chemical potentials. This expression can be given the form of Equation (13) with η defined as

$$\eta = \frac{\partial \varepsilon_B}{\partial \mu_B}\left[\frac{\partial \varepsilon_B}{\partial \mu_B} + \frac{\partial \varepsilon_\chi}{\partial \mu_\chi}\frac{d\mu_\chi}{d\mu_B}\right]^{-1}. \quad \text{(B2)}$$

The thermodynamic identities $n_B = \frac{\partial p_B}{\partial \mu_B}$ and $\varepsilon_B = \mu_B n_B - p_B$ can be used in order to obtain $\frac{\partial \varepsilon_B}{\partial \mu_B} = \mu_B \frac{\partial n_B}{\partial \mu_B}$. We similarly obtain $\frac{\partial \varepsilon_\chi}{\partial \mu_\chi} = \mu_\chi \frac{\partial n_\chi}{\partial \mu_\chi}$. Within stellar interiors chemical potential of two components scale proportionally to each other (Ivanytskyi et al. 2020). This allows us to conclude that $\frac{d\mu_\chi}{d\mu_B} = \frac{\mu_\chi}{\mu_B} = \xi$. Thus, Equation (B2) becomes

$$\eta = \frac{\partial n_B}{\partial \mu_B}\left[\frac{\partial n_B}{\partial \mu_B} + \xi^2\frac{\partial n_\chi}{\partial \mu_\chi}\right]^{-1}. \quad \text{(B3)}$$

Mechanical stability of BM and DM requires $\frac{\partial n_B}{\partial \mu_B} > 0$ and $\frac{\partial n_\chi}{\partial \mu_\chi}$, respectively. In this case η by construction is limited to the interval $\eta \in [0,\ 1]$. The lower edge of this interval $\eta = 0$ is obtained at $\mu_B = 0$, which corresponds to the absence of BM. On the other hand, the case of pure BM is obtained at $\mu_\chi = 0$ yielding $\eta = 1$.

Appendix C
Scan over Boson Mass and the Interaction Scale

Figure 5 presents a scan over model parameters for the IST EoS (upper row), DD2 EoS (middle row), and DD2Λ EoS (bottom row) for fixed DM fractions of 1%, 3%, and 5%.

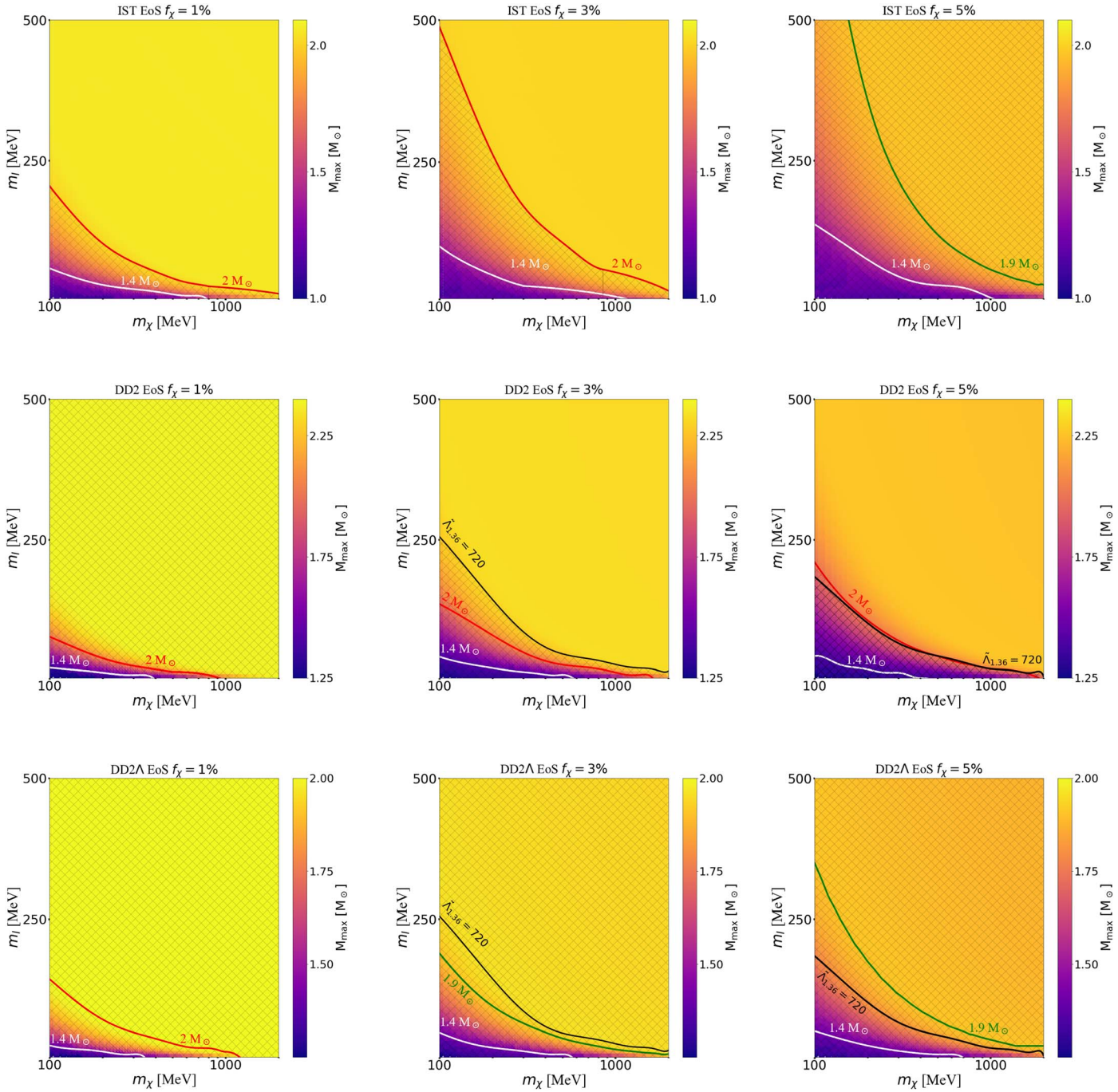

Figure 5. Upper row: parameter space in the m_I–m_χ plane calculated for the IST EoS and different values of DM fraction, 1% (left panel), 3% (middle panel), and 5% (right panel). The color represents the total maximum gravitational mass of DM-admixed NSs. The white and red curves correspond to stars with the total maximum gravitational mass equal to 1.4 and 2 $M_\odot$, respectively. For a DM fraction of 5% (see the right panel) the maximum mass do not reach 2 $M_\odot$; thus, we show 1.9 $M_\odot$ configurations in green. Shaded areas correspond to the non-allowed regions of parameters, whereas simultaneously the astrophysical and GW constraints are not fulfilled. Middle row: the same as in the upper row, but calculated for DD2 EoS. The tidal deformability constraint $\tilde{\Lambda}_{1.36} = 720$ (90% credible interval) is shown as a black curve. All the area above this curve is consistent with the GW170817 tidal deformability constraint (Abbott et al. 2019b). The 1% DM case is not consistent with the tidal deformability constraint for all values of m_I and m_χ. Lower row: the same as in the middle and upper rows, but calculated for DD2Λ EoS.

ORCID iDs

Edoardo Giangrandi https://orcid.org/0000-0001-9545-466X
Violetta Sagun https://orcid.org/0000-0001-5854-1617
Oleksii Ivanytskyi https://orcid.org/0000-0002-4947-8721
Constança Providência https://orcid.org/0000-0001-6464-8023
Tim Dietrich https://orcid.org/0000-0003-2374-307X

References

Abbott, B. P., Abbott, R., Abbott, T. D., et al. 2017a, PhRvL, 119, 161101
Abbott, B. P., Abbott, R., Abbott, T. D., et al. 2017b, ApJL, 848, L12
Abbott, B. P., Abbott, R., Abbott, T. D., et al. 2018, PhRvL, 121, 161101
Abbott, B. P., Abbott, R., Abbott, T. D., et al. 2019a, PhRvL, 123, 011102
Abbott, B. P., Abbott, R., Abbott, T. D., et al. 2019b, PhRvX, 9, 011001
Abbott, B. P., Abbott, R., Abbott, T. D., et al. 2020a, ApJL, 892, L3
Abbott, R., Abbott, T. D., Abraham, S., et al. 2020b, ApJL, 896, L44
Ahn, K.-J., & Shapiro, P. R. 2005, MNRAS, 363, 1092

Ángeles Pérez-García, M., Grigorian, H., Albertus, C., Barba, D., & Silk, J. 2022, PhLB, 827, 136937
Annala, E., Gorda, T., Kurkela, A., & Vuorinen, A. 2018, PhRvL, 120, 172703
Antoniadis, J., Freire, P. C. C., Wex, N., et al. 2013, Sci, 340, 448
Bailes, M., Barr, E., Bhat, N. D. R., et al. 2018, in MeerKAT Science: On the Pathway to the SKA (MeerKAT2016), 277 (Trieste: SISSA), 11
Bauswein, A., Guo, G., Lien, J.-H., Lin, Y.-H., & Wu, M.-R. 2023, PhRvD, 107, 083002
Bauswein, A., Just, O., Janka, H.-T., & Stergioulas, N. 2017, ApJL, 850, L34
Baym, G., Pethick, C., & Sutherland, P. 1971, ApJ, 170, 299
Bell, N. F., Busoni, G., Motta, T. F., et al. 2021, PhRvL, 127, 111803
Bell, N. F., Busoni, G., Robles, S., & Virgato, M. 2020, JCAP, 2020, 028
Bertone, G., & Fairbairn, M. 2008, PhRvD, 77, 043515
Bezares, M., Viganò, D., & Palenzuela, C. 2019, PhRvD, 100, 044049
Bower, G. C., Chatterjee, S., Cordes, J., et al. 2018, in ASP Conf. Ser. 517, Science with a Next Generation Very Large Array, ed. E. Murphy (San Francisco, CA: ASP), 793
Brading, K., & Brown, H. R. 2000, arXiv:hep-th/0009058
Bramante, J., Fukushima, K., & Kumar, J. 2013, PhRvD, 87, 055012
Bramante, J., & Linden, T. 2014, PhRvL, 113, 191301
Burger, J. D., Zavala, J., Sales, L. V., et al. 2022, PhRvL, 129, 191103
Buschmann, M., Dessert, C., Foster, J. W., Long, A. J., & Safdi, B. R. 2022, PhRvL, 128, 091102
Cassano, R., Fender, R., Ferrari, C., et al. 2018, arXiv:1807.09080
Chang, J. H., Essig, R., & McDermott, S. D. 2018, JHEP, 09, 051
Ciarcelluti, P., & Sandin, F. 2011, PhLB, 695, 19
Clowe, D., Bradač, M., Gonzalez, A. H., et al. 2006, ApJL, 648, L109
Colpi, M., Shapiro, S. L., & Wasserman, I. 1986, PhRvL, 57, 2485
Das, A., Malik, T., & Nayak, A. C. 2022, PhRvD, 105, 123034
Das, H. C., Kumar, A., Kumar, B., et al. 2020b, MNRAS, 495, 4893
de Lavallaz, A., & Fairbairn, M. 2010, PhRvD, 81, 123521
Del Popolo, A., Le Delliou, M., & Deliyergiyev, M. 2020, Univ, 6, 222
Dengler, Y., Schaffner-Bielich, J., & Tolos, L. 2022, PhRvD, 105, 043013
Dexheimer, V., Gomes, R. O., Klähn, T., Han, S., & Salinas, M. 2021, PhRvC, 103, 025808
Dietrich, T., & Clough, K. 2019, PhRvD, 100, 083005
Di Giovanni, F., Sanchis-Gual, N., Cerdá-Durán, P., & Font, J. A. 2022, PhRvD, 105, 063005
Doroshenko, V., Suleimanov, V., Pühlhofer, G., & Santangelo, A. 2022, NatAs, 6, 1444
Ellis, J., Hektor, A., Hütsi, G., et al. 2018a, PhLB, 781, 607
Ellis, J., Hütsi, G., Kannike, K., et al. 2018b, PhRvD, 97, 123007
Emma, M., Schianchi, F., Pannarale, F., Sagun, V., & Dietrich, T. 2022, Particles, 5, 273
Essick, R., & Landry, P. 2020, ApJ, 904, 80
Fattoyev, F. J., Horowitz, C. J., Piekarewicz, J., & Reed, B. 2020, PhRvC, 102, 065805
Fonseca, E., Cromartie, H. T., Pennucci, T. T., et al. 2021, ApJL, 915, L12
Fortin, M., Avancini, S. S., Providência, C., & Vidaña, I. 2017, PhRvC, 95, 065803
Fortin, M., Providência, C., Raduta, A. R., et al. 2016, PhRvC, 94, 035804
Fortin, M., Raduta, A. R., Avancini, S., & Providência, C. 2020, PhRvD, 101, 034017
Gal, A., Hungerford, E. V., & Millener, D. J. 2016, RvMP, 88, 035004
Giudice, G. F., McCullough, M., & Urbano, A. 2016, JCAP, 2016, 001
Goldman, I., Mohapatra, R. N., Nussinov, S., Rosenbaum, D., & Teplitz, V. 2013, PhLB, 725, 200
Gresham, M. I., Lou, H. K., & Zurek, K. M. 2017, PhRvD, 96, 096012
Grill, F., Pais, H., Providência, C., Vidaña, I., & Avancini, S. S. 2014, PhRvC, 90, 045803
Hamaguchi, K., Nagata, N., & Yanagi, K. 2019, PhLB, 795, 484
Hinderer, T. 2008, ApJ, 677, 1216
Hinderer, T., Nissanke, S., Foucart, F., et al. 2019, PhRvD, 100, 06321
in't Zand, J. J. M., Bozzo, E., Qu, J., et al. 2019, SCPMA, 62, 029506
Ivanytskyi, A. I., Bugaev, K. A., Sagun, V. V., Bravina, L. V., & Zabrodin, E. E. 2018, PhRvC, 97, 064905
Ivanytskyi, O., & Blaschke, D. 2022, PhRvD, 105, 114042
Ivanytskyi, O., Sagun, V., & Lopes, I. 2020, PhRvD, 102, 063028
Kapusta, J. I., & Gale, C. 2006, Finite-temperature Field Theory: Principles and Applications (2nd ed.; Cambridge: Cambridge Univ. Press)
Karkevandi, D. R., Shakeri, S., Sagun, V., & Ivanytskyi, O. 2022, PhRvD, 105, 023001
Kouvaris, C. 2008, PhRvD, 77, 023006
Kouvaris, C. 2013, AdHEP, 2013, 856196
Kouvaris, C., & Nielsen, N. G. 2015, PhRvD, 92, 063526
Kouvaris, C., & Tinyakov, P. 2010, PhRvD, 82, 063531
Leung, K.-L., Chu, M.-c., & Lin, L.-M. 2022, PhRvD, 105, 123010
Maselli, A., Pnigouras, P., Nielsen, N. G., Kouvaris, C., & Kokkotas, K. D. 2017, PhRvD, 96, 023005
Miao, Z., Zhu, Y., Li, A., & Huang, F. 2022, ApJ, 936, 69
Miller, M. C., Lamb, F. K., Dittmann, A. J., et al. 2019, ApJL, 887, L24
Miller, M. C., Lamb, F. K., Dittman, A. J., et al. 2021, ApJL, 918, L28
Mills, C., Tiwari, V., & Fairhurst, S. 2018, PhRvD, 97, 104064
Moore, B. 1994, Natur, 370, 629
Nelson, A. E., Reddy, S., & Zhou, D. 2019, JCAP, 2019, 012
Oppenheimer, J. R., & Volkoff, G. M. 1939, PhRv, 55, 374
Page, D., Lattimer, J. M., Prakash, M., & Steiner, A. W. 2004, ApJS, 155, 623
Pérez-García, M. Á., & Silk, J. 2012, PhLB, 711, 6
Petraki, K., & Volkas, R. R. 2013, IJMPA, 28, 1330028
Punturo, M., Abernathy, M., Acernese, F., et al. 2010, CQGra, 27, 194002
Raaijmakers, G., Greif, S. K., Hebeler, K., et al. 2021, ApJL, 918, L29
Raaijmakers, G., Greif, S. K., Riley, T. E., et al. 2020, ApJL, 893, L21
Randall, S. W., Markevitch, M., Clowe, D., Gonzalez, A. H., & Bradac, M. 2008, ApJ, 679, 1173
Ray, P. S., Arzoumanian, Z., Ballantyne, D., et al. 2019, arXiv:1903.03035
Regge, T., & Wheeler, J. A. 1957, PhRv, 108, 1063
Riley, T. E., Watts, A. L., Bogdanov, S., et al. 2019, ApJL, 887, L21
Riley, T. E., Watts, A. L., Ray, P. S., et al. 2021, ApJL, 918, L27
Romani, R. W., Kandel, D., Filippenko, A. V., Brink, T. G., & Zheng, W. 2021, ApJL, 908, L46
Romani, R. W., Kandel, D., Filippenko, A. V., Brink, T. G., & Zheng, W. 2022, ApJL, 934, L18
Rüter, H. R., Sagun, V., Tichy, W., & Dietrich, T. 2023, arXiv:2301.03568
Rutherford, N., Raaijmakers, G., Prescod-Weinstein, C., & Watts, A. 2023, PhRvD, 107, 103051
Sagun, V. V., Bugaev, K. A., Ivanytskyi, A. I., et al. 2018, EPJA, 54, 100
Sagun, V. V., Bugaiev, K. A., Ivanytskyi, A. I., Oliinychenko, D. R., & Mishustin, I. N. 2017, EPJWC, 137, 09007
Sagun, V., Giangrandi, E., Dietrich, T, et al. 2023, arXiv:2306.12326
Sagun, V., Giangrandi, E., Ivanytskyi, O., Lopes, I., & Bugaev, K. 2022, in Particles and Nuclei International Conference 2021 (PANIC2021), 380 (Trieste: SISSA), 313
Sagun, V., Lopes, I., & Ivanytskyi, A. 2019a, NuPhA, 982, 883
Sagun, V. V., Lopes, I., & Ivanytskyi, A. I. 2019b, ApJ, 871, 157
Sagun, V., Panotopoulos, G., & Lopes, I. 2020, PhRvD, 101, 063025
Sedrakian, A. 2016, PhRvD, 93, 065044
Sedrakian, A. 2019, PhRvD, 99, 043011
Tan, H., Dexheimer, V., Noronha-Hostler, J., & Yunes, N. 2022, PhRvL, 128, 161101
Tan, H., Noronha-Hostler, J., & Yunes, N. 2020, PhRvL, 125, 261104
Tews, I., Pang, P. T. H., Dietrich, T., et al. 2021, ApJL, 908, L1
Tolman, R. C. 1939, PhRv, 55, 364
Tsokaros, A., Ruiz, M., & Shapiro, S. L. 2020, ApJ, 905, 48
Typel, S., Ropke, G., Klahn, T., Blaschke, D., & Wolter, H. H. 2010, PhRvC, 81, 015803
Typel, S., & Wolter, H. H. 1999, NuPhA, 656, 331
Watts, A., Espinoza, C. M., Xu, R., et al. 2015, PoS, 215, 043
Yagi, K., & Yunes, N. 2016, CQGra, 33, 13LT01
Zhang, N.-B., & Li, B.-A. 2020, ApJ, 902, 38
Zurek, K. M. 2014, PhR, 537, 91